Wave-front phase estimation from Fourier intensity measurements

J. N. Cederquist, J. R. Fienup, C. C. Wackerman, S. R. Robinson, and D. Kryskowski

Advanced Concepts Division, Environmental Research Institute of Michigan, P.O. Box 8618, Ann Arbor, Michigan 48107

A novel wave-front sensor that estimates phase from Fourier intensity measurements is described, and an explicit expression is found and numerically evaluated for the Cramér–Rao lower bound on integrated rms wave-front phase estimation error. For comparison, turbulence-aberrated wave-front phases and corresponding noisy Fourier intensity measurements were computer simulated. An iterative phase-retrieval algorithm was then used to estimate the phase from the Fourier intensity measurements and knowledge of the shape of an aperture through which the wave front passed. The simulation error approaches the lower bound asymptotically as the noise is reduced.

1. INTRODUCTION

The Fourier intensity wave-front sensor, introduced in this paper, operates by using a lens or a mirror to Fourier transform the field in the sensor aperture to a measurement plane where the intensity (squared modulus) of the Fourier transform of the wave front is detected as depicted in Fig. 1. In most cases of practical interest, the atmospheric phase is related uniquely to the Fourier- (focal-) plane intensity measurements.[1] The wave front may then be reconstructed from the Fourier intensity by using an iterative Fourier-transform (phase-retrieval) algorithm.[2,3] Previously described methods of wave-front sensing by phase retrieval[4] assumed knowledge of the wave-front intensity in both the aperture plane and the Fourier (focal) plane, whereas in this paper we assume only knowledge of the Fourier-plane intensity and of the shape of the entrance aperture.

The Cramér–Rao method can be used to find a lower bound on the rms error of a phase estimate.[5,6] The bound does not depend on the algorithm used for computing the phase estimate from the measured data. It gives, instead, a measure of estimation performance for the chosen measurements and the underlying statistics that cannot be exceeded by any algorithm.

In Section 2, the Fourier intensity wave-front sensor is described. In Section 3, the Cramér–Rao lower bound is found for the Fourier intensity wave-front sensor. In Section 4, the error lower bound is compared with the phase estimate error obtained by reconstructing the phase from computer-simulated Fourier intensity data. Conclusions and suggestions for further studies are given in Section 5.

2. FOURIER INTENSITY WAVE-FRONT SENSOR

The Fourier intensity wave-front sensor consists simply of (1) a shaped aperture through which the wave front of interest passes, (2) a Fourier-transform lens that produces the Fourier transform of the apertured wave front in its back focal plane, and (3) a detector array in the focal plane that detects the intensity of that Fourier transform. The Fourier modulus, which is the square root of the measured Fourier intensity, and knowledge of the shape of the aperture are then used to reconstruct the wave fronts in the aperture and Fourier domains by the iterative (Fourier) transform algorithm.[2,3,7] The iterative Fourier-transform algorithm involves iteratively transforming back and forth between the Fourier domain, where the measured data are used, and the aperture domain, where knowledge of the shape of the aperture is used. Several versions of the algorithm are useful, including the error-reduction algorithm, which has a convergence proof but in practice converges slowly, and the hybrid input–output algorithm, which has no convergence proof but in practice converges much more rapidly. Further details on the iterative Fourier-transform algorithm can be found in Refs. 2, 3, and 7. The iterative Fourier-transform algorithm attempts to find a Fourier-transform pair that is simultaneously consistent with both the Fourier-domain data and the aperture-domain shape constraint (that no energy fall outside the aperture) and thereby retrieves the wave-front phase. It has been shown that, for certain favorable aperture shapes, the algorithm in practice converges reliably to the correct solution.[3] A Fresnel transform can also be used in place of the Fourier transform.

The Fourier intensity wave-front sensor makes no assumptions about the aperture-plane intensity, nor does it require the measurement of this intensity, as do some other wave-front sensors.[2,4,7] Thus the Fourier intensity wave-front sensor is a particularly simple optical system that detects the wave-front (transformed) intensity in an efficient manner. Its principal drawback is the requirement of an aperture shape for which the iterative Fourier-transform algorithm works well,[3] such as a polygon having no parallel sides (a triangle being the best example) or an aperture having two or more separated subapertures. If the desired area of the reconstructed wave front differs greatly from any aperture shape that is favorable for reconstruction, then either (1) the aperture could be made of a favorable shape that is larger than and includes the desired wave-front area or (2) the desired wave-front area could be subdivided into
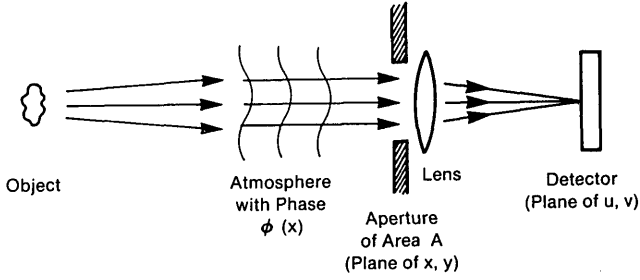
Fig. 1.   Model of the Fourier intensity wave-front sensor system.

two (or more) wave fronts, each having a favorable shape and each being Fourier transformed and detected separately in a two-channel (or multichannel) configuration.

3.   LOWER BOUND FOR THE FOURIER INTENSITY WAVE-FRONT SENSOR

In this section the lower bound for the Fourier intensity wave-front sensor is given. The approach used here is similar to that used previously[6] to analyze a shearing interferometer.

If we denote the true wave-front phase by $\phi(\mathbf{x})$, where $\mathbf{x}$ is a two-dimensional vector, and the phase estimate by $\tilde{\phi}(\mathbf{x})$, then the integrated mean-squared error, e^2, of the phase estimate is

$$e^2 = \frac{1}{A}\int_A E\{[\tilde{\phi}(\mathbf{x}) - \phi(\mathbf{x})]^2\}d\mathbf{x}, \tag{1}$$

where $E\{\cdot\}$ denotes the expected value and A is the area of the sensor input aperture. It can be proved that e^2 has a Cramér–Rao lower bound, e_0^2, given by[5]

$$e_0^2 = \frac{1}{A}\int_A J^{-1}(\mathbf{x}, \mathbf{x})d\mathbf{x}. \tag{2}$$

The inverse information kernel $J^{-1}(\mathbf{x}, \mathbf{x})$ is defined by the integral equation[6]

$$J^{-1}(\mathbf{x}, \mathbf{y}) + \int_A\int_A J^{-1}(\mathbf{x}, \mathbf{p})R(\mathbf{p}, \mathbf{q})K(\mathbf{q} - \mathbf{y})d\mathbf{p}d\mathbf{q} = K(\mathbf{x} - \mathbf{y}), \tag{3}$$

where

$$R(\mathbf{x}, \mathbf{y}) = (4\eta^2 T^2/N)\exp[-2K(0)]\text{Re}\Bigg\{\int_P\int_A\int_A h(\mathbf{u}, \mathbf{x})$$

$$\times h^*(\mathbf{u}, \mathbf{p})M(\mathbf{x}, \mathbf{p})\exp[K(\mathbf{x} - \mathbf{p}) + K(\mathbf{y} - \mathbf{q})]$$

$$\times \{h^*(\mathbf{u}, \mathbf{y})h(\mathbf{u}, \mathbf{q})M^*(\mathbf{y}, \mathbf{q})\exp[K(\mathbf{x} - \mathbf{y})$$

$$- K(\mathbf{x} - \mathbf{q}) - K(\mathbf{y} - \mathbf{p}) + K(\mathbf{p} - \mathbf{q})] - h(\mathbf{u}, \mathbf{y})$$

$$\times h^*(\mathbf{u}, \mathbf{q})M(\mathbf{y}, \mathbf{q})\exp[-K(\mathbf{x} - \mathbf{y}) + K(\mathbf{x} - \mathbf{q})$$

$$+ K(\mathbf{y} - \mathbf{p}) - K(\mathbf{p} - \mathbf{q})]\}d\mathbf{u}d\mathbf{p}d\mathbf{q}\Bigg\}; \tag{4}$$

η is the detector quantum efficiency, T is the detector integration time; $K(\mathbf{x})$ is the covariance of the assumed zero-mean, Gaussian-distributed phase $\phi(\mathbf{x})$; $h(\mathbf{u}, \mathbf{x})$ is the coherent impulse response of the wave-front sensor, where $\mathbf{u}$ is a two-dimensional vector in the measurement region P; $M(\mathbf{x}, \mathbf{x}')$ is the mutual intensity of the wave front in the sensor

input aperture; and zero-mean, spatially uncorrelated, Gaussian-distributed additive noise with variance N is assumed. Further explanation of Eqs. (2)–(4) is given in Ref. 6 and in Appendix A.

The inverse information kernel $J^{-1}(\mathbf{x}, \mathbf{y})$, when evaluated for $\mathbf{x} = \mathbf{y}$, represents a lower bound on the mean-squared error of the estimate of the phase ϕ at the point $\mathbf{x}$. The integral equation determines J^{-1} in terms of the covariance K of the phase and the complicated expression [Eq. (4)] for R, which in turn includes the detector quantum efficiency, the integration time, the variance of the detector noise, the mutual intensity of the aperture field that is due to the object, and the wave-front sensor impulse response.

For the Fourier intensity wave-front sensor, the impulse response is

$$h(\mathbf{u}, \mathbf{x}) = [W(\mathbf{x})/i\lambda F]\exp(-i2\pi\mathbf{u}\cdot\mathbf{x}/\lambda F), \tag{5}$$

where $W(\mathbf{x})$ is a real-valued aperture mask, λ is the wavelength, and F is the lens focal length. Each point $\mathbf{x}$ in the aperture plane results in a tilted plane wave in the detection plane, with tilt proportional to $\mathbf{x}$. A mask defining the aperture is included in the analysis at this point because aperture shape has been shown to affect estimation-algorithm (phase-retrieval) performance.[3]

To proceed, Eq. (5) is substituted into Eq. (4). It is a good assumption that the measurement region P (i.e., the entire detector array) is sufficiently large that

$$(\lambda F)^{-2}\int_P \exp(-i2\pi\mathbf{u}\cdot\mathbf{x}/\lambda F)d\mathbf{u} = \delta(\mathbf{x}). \tag{6}$$

This assumption is equivalent to stating that the measurement plane is large enough so that all the light in the Fourier transform of the aperture field is detected. The simulations (see Section 4) showed that this does not lead to unreasonable detector areas. Using the delta functions to perform the $\mathbf{q}$ integration gives

$$R(\mathbf{x}, \mathbf{y})$$

$$= [4\eta^2 T^2/(\lambda F)^2 N]\,W(\mathbf{x})W(\mathbf{y})\exp[-2K(0) + 2K(\mathbf{x} - \mathbf{y})]$$

$$\times \text{Re}\Bigg\{\int_A W(\mathbf{p})M(\mathbf{x}, \mathbf{p})\exp[2K(\mathbf{x} - \mathbf{p}) + 2K(\mathbf{y} - \mathbf{p})]$$

$$\times \{W(\mathbf{y} - \mathbf{x} + \mathbf{p})M^*(\mathbf{y}, \mathbf{y} - \mathbf{x} + \mathbf{p})$$

$$\times \exp[-3K(\mathbf{y} - \mathbf{p}) - K(2\mathbf{x} - \mathbf{y} - \mathbf{p})]$$

$$- W(\mathbf{y} + \mathbf{x} - \mathbf{p})M(\mathbf{y}, \mathbf{y} + \mathbf{x} - \mathbf{p})$$

$$\times \exp[-3K(\mathbf{x} - \mathbf{y}) - K(\mathbf{x} + \mathbf{y} - 2\mathbf{p})]\}d\mathbf{p}\Bigg\}. \tag{7}$$

This expression is valid for any object, aperture shape, or atmospheric covariance, but it is also quite complicated.

To proceed further, a Gaussian atmospheric covariance,

$$K(\mathbf{x} - \mathbf{y}) = \sigma_\phi^2 \exp(-|\mathbf{x} - \mathbf{y}|^2/r_\phi^2), \tag{8}$$

was assumed, where σ_ϕ^2 is the phase variance and r_ϕ is the correlation length of the phase. These parameters can be related to the commonly used atmospheric coherence length r_0 (Ref. 8) by using standard formulas.[9] It can be shown that $r_0 \simeq 1.86r_\phi/\sigma_\phi$.

It was also assumed for simplicity that the extended object

is incoherent and has a Gaussian spatial-intensity distribution. The mutual intensity is then

$$M(\mathbf{x}, \mathbf{y}) = I \exp(-|\mathbf{x} - \mathbf{y}|^2/L^2), \qquad (9)$$

where I is the intensity and L is the field coherence length in the sensor aperture. (The field in the aperture that is due to an incoherent source is, by the van Cittert–Zernike theorem, partially coherent.[10])

It was found by extensive numerical evaluation of Eq. (7) that, for the most likely aperture shapes (e.g., circle, square, triangle), a good approximation is

$$R(\mathbf{x}, \mathbf{y}) \simeq [4\eta^2 T^2 I^2 A_0/(\lambda F)^2 N] W(\mathbf{x}) W(\mathbf{y})$$

$$\times \exp\{-2\sigma_\phi^2[1 - \exp(-|\mathbf{x} - \mathbf{y}|^2/r_\phi^2)]\}, \quad (10)$$

where $A_0 = \min(A, \pi L^2)$. The aperture mask $W(\mathbf{x})$ dependence can also be dropped, since aperture shape does not seem to be a major factor. A further approximation (shown numerically to be good for $\sigma_\phi > \pi/3$) can also be made:

$$R(\mathbf{x}, \mathbf{y}) \simeq [4\eta^2 T^2 I^2 A_0/(\lambda F)^2 N] \exp(-2\sigma_\phi^2 |\mathbf{x} - \mathbf{y}|^2/r_\phi^2). \quad (11)$$

(This approximation relies on the fact that, for $\sigma_\phi > \pi/3$, the exponential has a nonnegligible value only when $|\mathbf{x} - \mathbf{y}|^2/r_\phi^2$ is small.) R is now a function of $(\mathbf{x} - \mathbf{y})$, so Eq. (3) can be solved by Fourier methods.[6] Equation (17) of Ref. 6 gives a general solution. When the Fourier transforms of $K(\mathbf{x} - \mathbf{y})$ [Eq. (20) of Ref. 6] and $R(\mathbf{x} - \mathbf{y})$ are substituted into Eq. (17) of Ref. 6 and the angular integration is performed in the Fourier domain [see Eq. (18) of Ref. 6], the result for the lower bound for the Fourier intensity wave-front sensor is

$$e_0^2 = 2\sigma_\phi^2 \int_0^\infty \frac{f \exp(-f^2)}{1 + P \exp\{-f^2[1 + (2\sigma_\phi^2)^{-1}]\}} \, df, \quad (12)$$

where

$$P = 2\eta^2 T^2 I^2 A_0 (\pi r_\phi^2)^2 / [(\lambda F)^2 N]. \qquad (13)$$

Although Eq. (12) can not be evaluated analytically, a useful expression based on numerical investigations is

$$e_0^2 \simeq \sigma_\phi^2 \frac{\ln(1 + P')}{P'}, \qquad (14)$$

where

$$P' = P/[1 + (2\sigma_\phi^2)^{-1}]. \qquad (15)$$

Equation (14) is obtained by first replacing the $\exp(-f^2/2\sigma_\phi^2)$ term in Eq. (12) by its average value (f in the range from 0 to ∞) when weighted by $f \exp(-f^2)$,

$$\frac{\int_0^\infty \exp[-f^2(2\sigma_\phi^2)^{-1}]\exp(-f^2)f df}{\int_0^\infty \exp(-f^2)f df} = \frac{1}{1 + (2\sigma_\phi^2)^{-1}}, \quad (16)$$

and then integrating the resulting expression.

In what follows we develop an alternative expression for P in terms of photon rates with equivalent noise. As the ratio of the phase coherence length r_0 ($\simeq 1.86 r_\phi/\sigma_\phi$) to the sensor aperture diameter D decreases below unity, the intensity distribution in the measurement plane increasingly breaks into a speckle cloud whose radius is approximately $\lambda F/r_0$. Energy conservation within the Fourier intensity sensor im-

plies that the product of the average aperture intensity I with the aperture area A must be approximately equal to the product of an average intensity I_{FT} of the speckle cloud times the area of a disk including most of the energy in the speckle cloud. The radius of the disk is approximately $\lambda F/r_0$, so

$$IA = I_{FT}\pi(\lambda F/r_0)^2. \qquad (17)$$

Using Eq. (17) to substitute for I in Eq. (13) gives

$$P = \frac{2\pi^4 \eta^2 T^2 I_{FT}^2 A_0 \sigma_\phi^4 (\lambda F)^2}{(1.86)^4 A^2 N}. \qquad (18)$$

The parameter P contains the ratio $\eta^2 T^2 I_{FT}^2/(N/2)$, which is the ratio of signal power to thermal noise power. (For the purpose of estimation theory, the signal is $\eta T I_{FT}$, so the signal power is $\eta^2 T^2 I_{FT}^2$.) Since wave-front sensors are often used in low-light-level conditions, the detectors used should ideally be shot-noise limited. P can therefore be reinterpreted as follows: The number of detected photons per unit area is

$$s = \eta T I_{FT}/h\nu, \qquad (19)$$

where η is the detector quantum efficiency, T is the integration time, I_{FT} is the average intensity at the detector, h is Planck's constant, and $h\nu$ is the energy of a photon. For photon (shot) noise having Poisson statistics, the noise variance is equal to the mean number of photons, and so the noise power is

$$N_s = \eta T I_{FT}/h\nu. \qquad (20)$$

In Eq. (18), for the case of photon noise the ratio of signal power to noise power, $(\eta T I_{FT})^2/(N/2)$, should therefore be replaced by
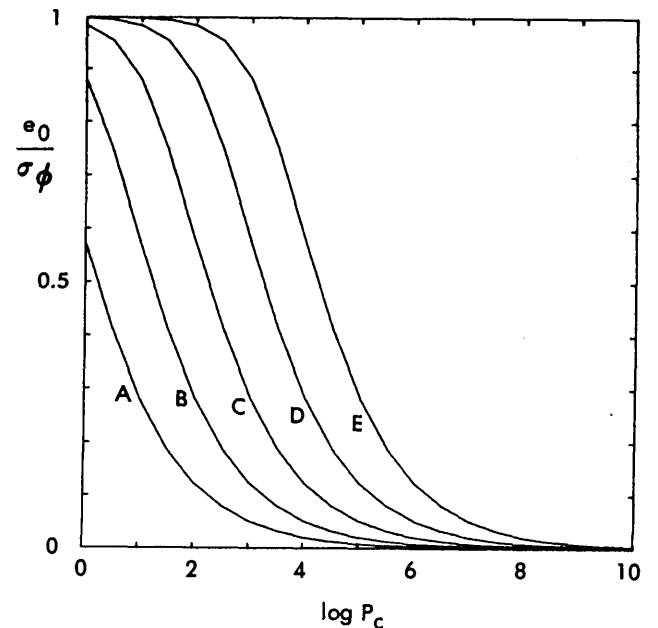
Fig. 2. Fourier intensity wave-front sensor normalized lower bound e_0/σ_ϕ versus light level P_c for $\sigma_\phi = \pi/2$ and (curve A) a point object and (curves B–E) extended objects with ratios of the field coherence area πL^2 to the sensor aperture area A of 10^{-1}, 10^{-2}, 10^{-3}, and 10^{-4}, respectively.
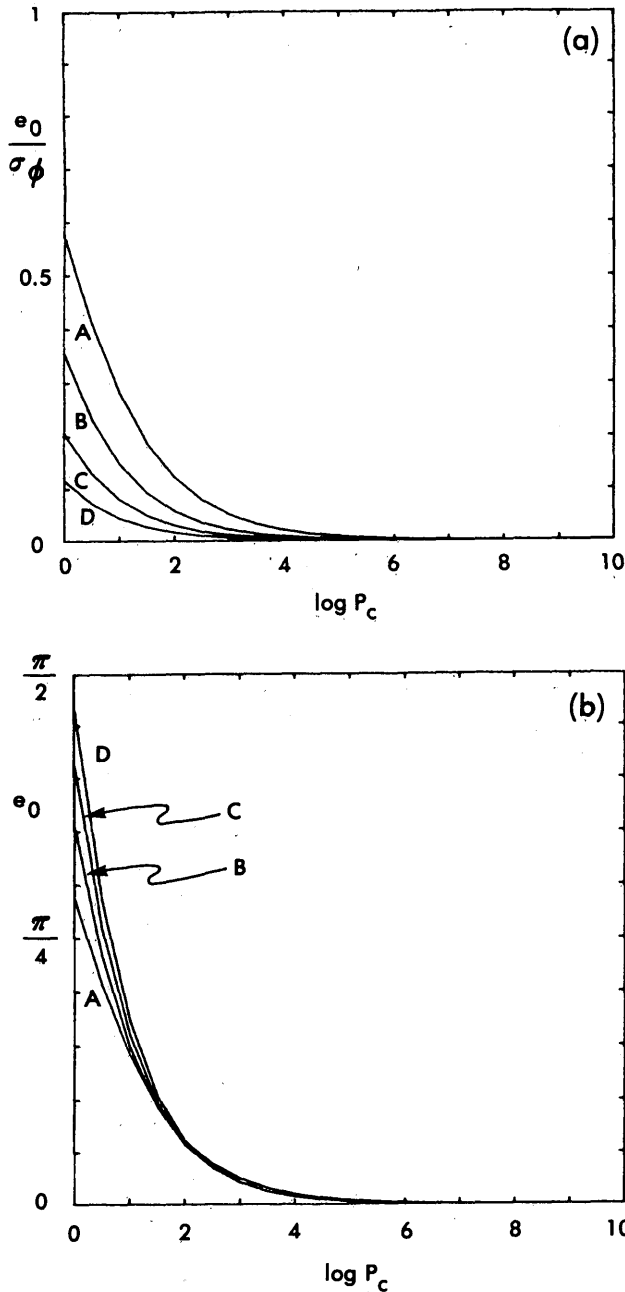
Fig. 3.   Fourier intensity wave-front sensor lower bound versus P_c for a point object and σ_ϕ of (curve A) $\pi/2$, (curve B) π, (curve C) 2π, and (curve D) 4π.   (a) Normalized lower bound e_0/σ_ϕ; (b) absolute lower bound e_0.

$$s^2/N_s = \eta T I_{FT}/\hbar\nu, \tag{21}$$

giving

$$P = \frac{\pi^4 \eta T I_{FT} A_0 \sigma_\phi^4 (\lambda F)^2}{(1.86)^4 A^2 \hbar\nu}. \tag{22}$$

Using Eq. (17) to convert I_{FT} back to I gives

$$P = \frac{\pi^2 \eta T I A_0 \sigma_\phi^2 (\pi r_\phi^2)}{(1.86)^2 A \hbar\nu}. \tag{23}$$

Further simplification can be obtained by defining an atmospheric coherence cell to be of area πr_ϕ^2 and noting that

the number of detected photons per coherence cell in time T is

$$P_c = \pi r_\phi^2 \eta T I/\hbar\nu. \tag{24}$$

The parameter P then becomes

$$P = 2.87 \sigma_\phi^2 P_c A_0/A. \tag{25}$$

Note that the dependence of the lower bound on r_0 is through the parameter P_c: the error lower bound increases as r_0 decreases.

By numerical integration of Eq. (12), e_0 was computed for various values of σ_ϕ, P_c, and A_0/A. The dependence of e_0 on light level is shown in Fig. 2, in which the normalized lower bound e_0/σ_ϕ is plotted versus P_c for the case of a point object ($L \to \infty$, $A_0 = A$) and various extended objects. In all cases, $\sigma_\phi = \pi/2$ was used. As expected, the error lower bound decreases with increasing light level per coherence cell and increases with increasing object width. e_0/σ_ϕ and e_0 are plotted versus P_c in Figs. 3(a) and 3(b), respectively, for various values of σ_ϕ for the case of a point object. The normalized lower bound improves as σ_ϕ increases, but the absolute lower bound e_0 becomes higher, as is expected.

4. COMPARISON OF ERROR BOUNDS WITH SIMULATED SENSOR-ALGORITHM PERFORMANCE

Computer simulations of the Fourier intensity wave-front sensor plus the iterative Fourier-transform algorithm were performed. The Fourier intensity wave-front sensor was simulated by using a discrete version of Eq. (5). Point objects were used, and the atmospheric phase was simulated[6] as in Ref. 11. The Gaussian covariance of Eq. (8) is an adequate approximation to the simulated phase covariance, as shown in Fig. 4.

The generalized expressions for the Cramér–Rao lower bound given in Section 3 were developed under the assumption of zero-mean, Gaussian-distributed noise (i.e., a ther-
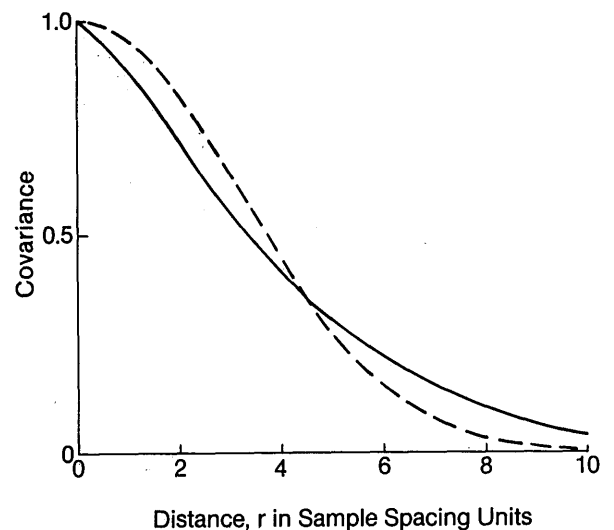
Fig. 4.   Comparison of simulated atmospheric phase covariance (solid curve) with Gaussian covariance (dashed curve) used in analysis.

mal-noise-limited detector). The lower bound expressions for the Fourier intensity wave-front sensor [Eqs. (12) and (13)] were developed for Gaussian-distributed noise but were interpreted to treat the case of Poisson-distributed noise (i.e., a shot-noise-limited detector) in Eq. (25). Uncorrelated, Poisson-distributed (shot) noise was added to the simulated Fourier intensity measurements.

The iterative Fourier transform algorithm, with a combination of the hybrid input–output and error-reduction approaches, was used to estimate the atmospheric phase.[2,3,7] In the aperture domain, the constraint that no energy fall outside the aperture was used. Square and triangular aperture area was kept the same for both aperture shapes. When the initial phase-estimate input to the algorithm was random, aperture shape did affect both the rate of convergence and the rms error, e, of the phase estimate. This is probably a result of the fact that the present algorithm converges better with some aperture shapes (triangles, for

example) than with others (squares, for example).[3] This result seems to be due to the fact that the phase-retrieval problem is guaranteed to have a unique solution for objects known to have a triangular shape.[12] To determine the best phase estimate that could ultimately be produced by an algorithm of this type, another set of simulations was performed, for which an initial phase estimate equal to the actual atmospheric phase was used. The algorithm was then allowed to converge to a phase estimate that was as consistent as possible with the noisy measurement-plane data and the shape constraint. In this case, the effect of the aperture shape was not significant. This seems to indicate that, although aperture shape is significant with regard to the present algorithms, it may not be significant if an improved algorithm is devised.

Figure 5 shows some sample simulation data for $\sigma_\phi = \pi/2$, $r_\phi = 6$ samples and a triangular aperture with 64 samples along each edge. This yields a ratio $D/r_0 \simeq 12.7$, in which D
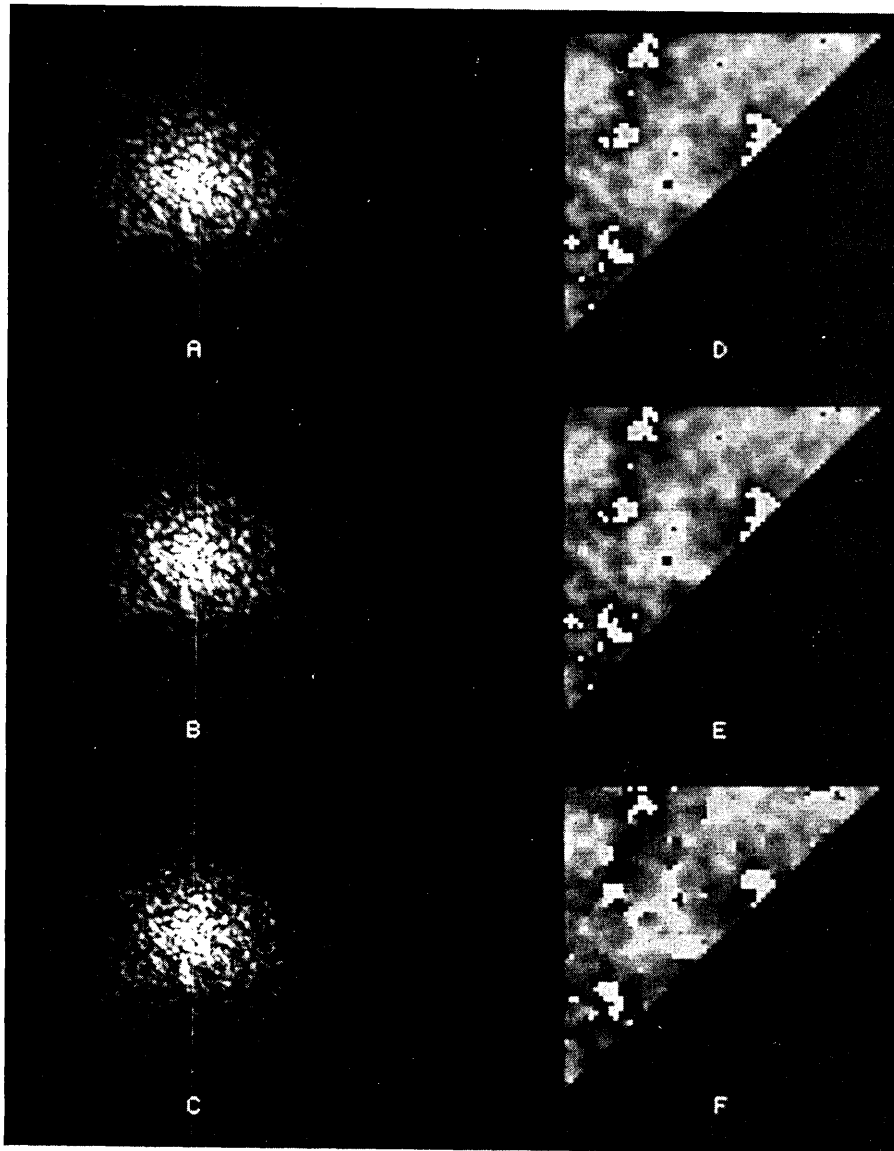
Fig. 5.   Fourier intensity wave-front sensor simulation for a point object, $\sigma_\phi = \pi/2$, and $D/r_0 \simeq 12.7$. Intensity in the measurement plane is shown (A) without noise and (B and C) for light levels P_c of 1.1×10^5 and 1.1×10^3 photons per coherence cell, respectively. Wave-front phases shown are (D) the actual phase and (E and F) phase estimates obtained from B and C, respectively, with a random initial phase estimate. The phases are wrapped with $-\pi$ phase (black) and $+\pi$ phase (white). Normalized errors e/σ_ϕ are (E) 0.059 and (F) 0.55.
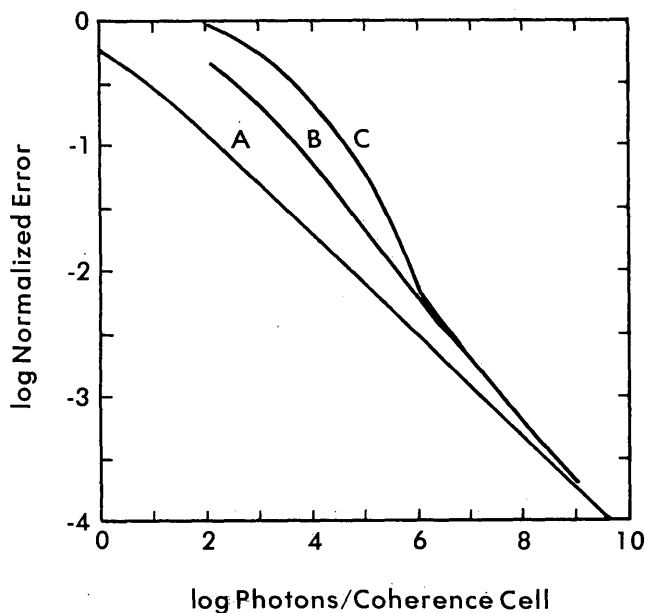
Fig. 6. Comparison of Fourier intensity wave-front sensor lower bound with simulation phase-estimate errors versus light level P_c for a point object, $\sigma = \pi/2$ and $D/r_0 \simeq 12.7$. Curve A represents the normalized lower bound e_0/σ_ϕ. Normalized simulation errors e/σ_ϕ are given for initial phase estimates of (curve B) the actual phase and (curve C) a random phase.

is the length of the diagonal of the triangular aperture. Figure 5A shows noiseless Fourier intensity data (in a 128×128 array), and Figs. 5B and 5C show the same data with shot noise for $P_c = 1.1 \times 10^5$ and $P_c = 1.1 \times 10^3$ photons per coherence cell (of area $\pi r_\phi{}^2$), respectively. Figure 5D shows the actual atmospheric phase. Figures 5E and 5F show phase estimates from the corresponding measurements in Figs. 5B and 5C, obtained by using random initial phase estimates. The normalized rms errors e/σ_ϕ are 0.059 and 0.55, respectively.

Figure 6 compares the Cramér–Rao lower bounds (curve A) with the simulation results. Actual rms errors are shown for the cases in which the initial phase estimate was the actual phase (curve B) and a random one (curve C). As the light level increases, both rms errors approach the lower bound asymptotically (i.e., $e/e_0 \to 1$). It should be noted that this behavior depends on the interpretation of the lower bound for Poisson noise [Eqs. (17)–(25)] and the approximate agreement between Eq. (8) and the simulated phase covariance (in particular, the determination of r_ϕ in the simulation data). The simulation error becomes large at low light levels because the phase-estimation algorithms did not use any information about the statistics of the atmospheric phase. The Cramér–Rao lower bounds approach the phase variance σ_ϕ because they do assume statistical information. The lower bounds approach zero at high light levels, but this limit would not be achieved in practice because of a number of effects (e.g., detector size, detector pattern noise, quantization noise, finite word length for computation) that are not present in the wave-front sensor model.

5. CONCLUSIONS

In summary, the Fourier intensity wave-front sensor operates by optically Fourier transforming the field in the sensor

aperture to a detector plane. The wave-front phase is then reconstructed from the Fourier intensity by a phase-retrieval algorithm. The analysis given here shows how the error lower bound depends on the phase variance $\sigma_\phi{}^2$, the light level P_c (in photons per coherence cell), and the ratio of the field coherence length L to the aperture diameter D. The lower bound does not depend strongly on the aperture shape. Total aperture diameter is important because the field over the entire aperture affects each point in the Fourier plane. As expected, sensor performance improves as the light level P_c increases, as r_0 increases, and as the field coherence length L increases (up to the aperture diameter D). An interesting result was that the dependence on coherence length L is equivalent to a reduction in light level P_c by a factor of $(L/D)^2$ [see Eq. (25)].

The Fourier intensity wave-front sensor was simulated numerically and the iterative Fourier-transform algorithm was used to obtain a phase estimate. The error lower bound and the computer simulation errors are given in Fig. 6 for a point object, an atmospheric phase variance $\sigma_\phi = \pi/2$, and $D/r_0 \simeq 12.7$. As shown, both the lower bound and the simulation errors decrease as the number of photons per coherence cell, P_c (i.e., the light level), increases. The simulation error approaches the lower bound asymptotically as P_c increases.

Further research should include (1) the study of cases in which the extended object is coherent or partially coherent rather than incoherent as was assumed here; (2) rederivation of the basic equations describing the application of the Cramér–Rao method to wave-front sensors for the case of Poisson (shot) noise; and (3) investigation of other performance measures, including estimation-theory lower bounds other than the Cramér–Rao bounds (e.g., the Bhattacharyya and the Barankin bounds), for evaluating wave-front sensors.

APPENDIX A: OUTLINE OF DERIVATION OF EQ. (4)

In Ref. 5 a derivation was given of the Cramér–Rao lower bound on the estimation error for one-dimensional functions. This derivation can be extended to two-dimensional functions such as the phase $\phi(\mathbf{x})$. In this appendix, an outline is given to enable the interested reader to derive Eq. (4). The first step is to make a Karhunen–Loeve expansion of $\phi(\mathbf{x})$,

$$\phi(\mathbf{x}) = \sum_{j=1}^{\infty} a_j g_j(\mathbf{x}), \tag{A1}$$

in which the functions $g_j(\mathbf{x})$ are the eigenfunctions of

$$\mu_j g_j(\mathbf{x}) = \int_A K(\mathbf{x} - \mathbf{y}) g_j(\mathbf{y}) \mathrm{d}\mathbf{y} \tag{A2}$$

with eigenvalues μ_j.

For a general wave-front sensor, the intensity in the detector plane is

$$I(\mathbf{a}, \mathbf{u}) = E\left(\int_A \int_A h(\mathbf{u}, \mathbf{x}) h^*(\mathbf{u}, \mathbf{y}) M(\mathbf{x}, \mathbf{y}) \right.$$
$$\left. \times \exp\{i[\phi(\mathbf{x}) - \phi(\mathbf{y})]\} \mathrm{d}\mathbf{x} \mathrm{d}\mathbf{y}\right), \tag{A3}$$

where Eq. (A1) is used to expand $\phi(\mathbf{x})$ and $\mathbf{a}$ is a vector composed of the a_j. Following the method described in Ref. 5, we obtain

$$\int_A \int_A R(\mathbf{x}, \mathbf{y}) g_j(\mathbf{x}) g_k(\mathbf{y}) \mathrm{d}\mathbf{x} \mathrm{d}\mathbf{y}$$

$$= E\left[\frac{2\eta^2 T^2}{N} \int_P \frac{\partial I(\mathbf{a}, \mathbf{u})}{\partial a_j} \frac{\partial I(\mathbf{a}, \mathbf{u})}{\partial a_k} \mathrm{d}\mathbf{u} \right]. \quad (A4)$$

Using the definition of $I(\mathbf{a}, \mathbf{u})$ in Eq. (A3) and the relation[5]

$$E\left(\exp\left\{ i \sum_{j=1}^{\infty} \mathbf{a}_j[g_j(x) - g_j(y)] \right\} \right) = \exp[-K(0) + K(\mathbf{x} - \mathbf{y})]$$

$$(A5)$$

gives, after much algebraic manipulation of Eq. (A4), the form of $R(\mathbf{x}, \mathbf{y})$ given in Eq. (4).

ACKNOWLEDGMENTS

REFERENCES

1. J. T. Foley and R. R. Butts, "Uniqueness of phase retrieval from intensity measurements," J. Opt. Soc. Am. **71**, 1008–1014 (1981).
2. J. R. Fienup, "Reconstruction and synthesis applications of an iterative algorithm," in *Transformations in Optical Signal Processing*, W. T. Rhodes, J. R. Fienup, and B. E. A. Saleh, eds., Proc. Soc. Photo-Opt. Instrum. Eng. **373**, 147–160 (1981).
3. J. R. Fienup, "Reconstruction of a complex-valued object from the modulus of its Fourier transform using a support constraint," J. Opt. Soc. Am. A **4**, 118–123 (1987).
4. R. A. Gonsalves, "Phase retrieval from modulus data," J. Opt. Soc. Am. **66**, 961–964 (1976).
5. H. Van Trees, *Detection, Estimation and Modulation Theory, Part I* (Wiley, New York, 1968), pp. 66–73, 79–85, 96–97, 178–182, 437–441.
6. J. N. Cederquist, S. R. Robinson, D. Kryskowski, J. R. Fienup, and C. C. Wackerman, "Cramér–Rao lower bound on wavefront sensor error," Opt. Eng. **25**, 586–592 (1986).
7. J. R. Fienup, "Phase retrieval algorithms: a comparison," Appl. Opt. **21**, 2758–2769 (1982).
8. D. L. Fried, "Statistics of a geometric representation of wavefront distortion," J. Opt. Soc. Am. **55**, 1427–1435 (1965).
9. W. Wolfe and G. Zissis, eds., *The Infrared Handbook* (Office of Naval Research, Washington, D.C., 1978), Chap. 6.
10. M. Born and E. Wolf, *Principles of Optics* (Pergamon, Oxford, 1975), p. 526.
11. B. L. McGlamery, "Computer simulation studies of compensation of turbulence degraded images," in *Image Processing*, J. C. Urbach, ed., Proc. Soc. Photo-Opt. Instrum. Eng. **74**, 225–233 (1976).
12. J. R. Fienup, "Reconstruction of objects having latent reference points," J. Opt. Soc. Am. **73**, 1421–1426 (1983).
13. J. N. Cederquist, S. R. Robinson, D. Kryskowski, J. R. Fienup, and C. C. Wackerman, "Cramér–Rao lower bound for Fourier modulus wavefront sensor," in *Digest of Topical Meeting on Signal Recovery and Synthesis II* (Optical Society of America, Washington, D.C., 1986), pp. 156–159.